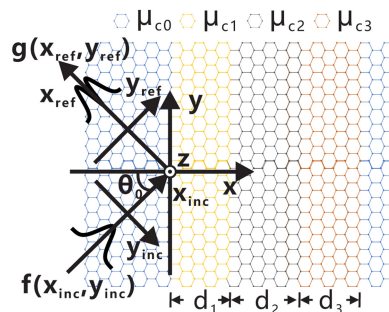


Efficient Optical Spatial First-Order Differentiator Based on Graphene-Based Metalines and Evolutionary Algorithms

Volume 12, Number 2, April 2020

Tian Zhang
Jia'nan Xie
Yihang Dan
Shuai Yu
Xu Han
Jian Dai
Kun Xu



DOI: 10.1109/JPHOT.2020.2966918

Efficient Optical Spatial First-Order Differentiator Based on Graphene-Based Metalines and Evolutionary Algorithms

Tian Zhang ¹, Jia'nan Xie,¹ Yihang Dan,¹ Shuai Yu,¹ Xu Han,²
Jian Dai ¹, and Kun Xu ¹

¹State Key Laboratory of Information Photonics and Optical Communications, Beijing
University of Posts and Telecommunications, Beijing 100876, P.R. China

²Huawei Technologies Co., Ltd, Shenzhen, Guangdong 518129, China

DOI:10.1109/JPHOT.2020.2966918

This work is licensed under a Creative Commons Attribution 4.0 License. For more information, see
<http://creativecommons.org/licenses/by/4.0/>

Manuscript received November 12, 2019; revised January 7, 2020; accepted January 10, 2020.
Date of publication January 26, 2020; date of current version March 9, 2020. This work was
supported in part by the National Natural Science Foundation of China under Grants 61705015,
61625104, 61431003, in part by The Beijing Municipal Science & Technology Commission under
Grants Z181100008918011; in part by The Fundamental Research Funds for the Central Universities
under Grants 2019RC15, 2018XKJC02; and in part the National Key Research and Development
program under Grant 2016YFA0301300. Corresponding author: Kun Xu (e-mail: xukun@bupt.edu.cn).

Abstract: We propose a novel optical spatial differentiator to perform the differentiation computation in terahertz region based on the graphene metalines, which consist of graphene layers with different widths and chemical potentials. The numerical simulation results show that when beam waist size $w > 1.9\lambda$, the metalines perform the first-order differentiation in the reflection spectrum with efficiency $> 97\%$, which can be theoretically demonstrated by using transfer matrix method. In order to further improve the performance of the differentiator, evolutionary algorithm, such as genetic algorithm, is used to inversely design the structure parameters and chemical potentials of graphene metalines. The optimization results show that some performance metrics of the differentiator, for example normalized root-mean-square deviation, are better than the previous structures. Obviously, the proposed graphene metalines combined with inverse design technology can achieve a high-performance optical spatial differentiator in terahertz region and provide a new way to design the photonics devices.

Index Terms: Optical differentiator, graphene, inverse design.

1. Introduction

As a high-performance solution to implement the fundamental mathematical operation, optical computing, which includes optical spatial computing [1]–[12] and optical time computing [13], [14], has attracted a great deal of attention. In comparison to traditional spatial computation, optical spatial computing has superiority in small size and fast response [15]. Optical spatial differentiation (OSD) is an important operation for real-time and parallel continuous data process, especially in image edge detection [16]. It has been demonstrated that OSD can be implemented by two different methods, namely Green's Function (GF) methods [1]–[4] and metasurfaces methods [6]–[8]. The metasurfaces methods have more degrees of freedom for the designing of optical analog devices, but their fabrications are relatively complex. In comparison to the bulky lens-based devices in the metasurfaces methods, the GF methods utilize a single surface [3], [7] or multilayer slab [1], [2],

[4], [5] to avoid the need of subblocks for Fourier transform and inverse Fourier transform. Thus, the complexity of fabrication and the dimensions of OSD are reduced, making it more feasible for on-chip integration [1], [5]. However, the OSD based on GF only performs well on a specific input condition, namely their performances are strictly limited by operation condition. Therefore, finding a reasonable structure whose physical parameters can be dynamically tuned to ensure an excellent performance is necessary.

Recently, graphene based metamaterials or metasurfaces have been applied in many photonics devices because they show great potential to manipulate electromagnetic waves [17]–[20]. And it has been demonstrated that the surface plasmons (SPs) excited on graphene metamaterials (metasurfaces) have exceptional electrical and optical properties, such as strong spatial confinement and high tunability [21]–[24]. Thus, plasmonic metasurfaces provide a promising avenue towards optical analog computing in deeply subwavelength volumes [25], [26]. In order to achieve ultra-compact differentiation and integration computing, graphene metalines, which are 1D counterparts of graphene metasurfaces, have been proposed to manipulate the amplitude and phase of an incident wave [6]. Similarly, metasurfaces blocks are suitably designed to modify conventional metamaterial-based optical integrator to obtain superior performance in low-frequency contents [27]. Obviously, we can use the high tunability of graphene metalines to meet the above requirements for the dynamic tuning of physical parameters. In addition, the high tunability of graphene metalines can be combined with inverse design technology to design a more efficient photonics device [28]–[30]. In general, inverse design is converted to the optimization problem which can be solved by gradient based methods (such as adjoint variable method (AVM) [31]–[32]), gradient free methods (such as genetic algorithm (GA) [33]–[37]) and model based methods (such as machine learning [38]–[40]). As a representative algorithm of gradient based methods, AVM not only designs linear devices but also optimizes for the nonlinear devices in frequency domain, but it requires physical background to derive the gradient of objective function [31]–[32]. Apart from the gradient-based methods, model based methods, such as artificial neural networks and random forest, are also used to inversely design the photonics devices [38]–[40]. However, in order to train the model whose inputs are physical parameters and outputs are electromagnetic responses, it requires a significant amount of time to generate the training instances and test instances [38]. In comparison to the gradient based methods and model based methods, gradient free methods, which depend on search strategy and evolutionary strategy, are simple, effective and parallelizable [33]–[37]. As a result, although GA easily falls into local optimum and demands tremendous computational time, it has been applied in the inverse design for many photonics devices, such as polarization beam splitters [33], polarization rotators [35], diodes [34], waveguide crossings [36], optical neural networks [37] and so on. It should be noted that previous researches pay little attention to the inverse design and performance optimization of OSD and graphene-based photonics devices, especially for the optimization of the physical parameters for graphene metasurfaces, such as chemical potential, relaxation time and so on.

In this study, we propose graphene metalines which can be used as a spatial first-order differentiator in terahertz region by manipulating graphene plasmons (GPs) waves. In order to achieve good performance for different input conditions, the chemical potentials of the graphene metalines are dynamically tuned. With the help of GA, the relationships between the physical parameters of graphene and performance metrics of the first-order differentiator are analyzed. The numerical simulation results exhibit that the differentiation performances of the OSD optimized by GA compete with the previous OSDs in [1], [6], [8]. And the normalized root-mean-square deviation (NRMSE) of the optimized OSDs are better than the previous structures. Obviously, the combination of the graphene-based OSD and inverse design technology promotes the development of OSD.

2. Device Design and Simulation Results

As shown in Fig. 1(a), our proposed OSD is based on graphene-based metalines, which consist of graphene layers with different widths and chemical potentials. The chemical potentials and widths of the graphene layers in this metalines are described by $\mu_{c,i}$ ($i = 0, 1, 2, 3$) and d_i ($i = 1, 2, 3$),

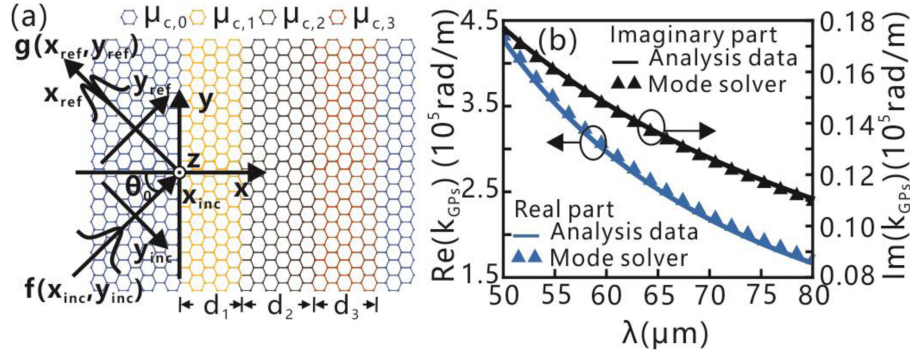


Fig. 1. (a) Schematic of the proposed graphene-based differentiator. The chemical potentials of the first-layer and last-layer graphene $\mu_{c,0}$ are fixed to 0.5 eV. (b) The wavenumber k_{GPs} of GPs when the chemical potentials of all graphene layers are 0.5 eV. Blue solid line and blue triangles (black solid line and black triangles) correspond to the real (imaginary) part of k_{GPs} calculated by Drude model and mode solver method with Lumerical Mode-solutions, respectively.

respectively. A Gaussian distribution GPs beam $f(x_{inc}, y_{inc})$ with transverse wave vector k_y propagates in the y_{inc} -direction. Then the GPs beam incidents on the interface of metalines at an angle θ_0 with respect to negative x axis. And the beam $g(x_{ref}, y_{ref})$ reflected from the graphene metalines, performs the first-order differentiation of the input beam. For this system, the y -component field has the form [11]

$$\begin{aligned} f(x_{inc}, y_{inc}) &= \exp(ik_{GPs,0}x_{inc})P_{inc}(y_{inc}) \\ &= \exp(ik_{GPs,0}x_{inc}) \int G(k_{y,inc}) \exp(ik_{y,inc}y_{inc}) dk_{y,inc} \end{aligned} \quad (1)$$

where $k_{GPs,0}$ is the wave vector of incident GPs beam, $P_{inc}(y_{inc})$ is the transverse profile of incident beam, and $G(k_{y,inc})$ is the spatial Fourier component of $P_{inc}(y_{inc})$. Here, we assume that the spectrum $G(k_{y,inc})$ ($|k_{y,inc}| \leq g$, where g is the angular spectrum width) is sufficiently narrow, so $g \ll k_{GPs,0}$. In this case, the beam can be represented as a superposition of GPs with different spatial frequency values $k_{y,inc} = k_{GPs,0} \sin(\theta)$, where θ is the angle between the GPs propagated direction and x_{inc} axis. It is easy to see that k_y can be described as $k_y = k_{GPs,0} \sin(\theta + \theta_0) \approx k_{y,inc} \cos \theta_0 + k_{GPs,0} \sin(\theta_0)$. The transformation of $G(k_{y,inc})$ for incident beam is described by the multiplication of the reflection coefficient $r(k_y)$. Thus, the transverse profile of reflection beam $P_{refl}(y_{refl})$ takes the form:

$$\begin{aligned} P_{refl}(y_{refl}) &= \int G(k_{y,inc}) r(k_y) \exp(ik_{y,inc}y_{refl}) dk_{y,inc} \\ &= IFT [G(k_{y,inc}) r(k_y)] \end{aligned} \quad (2)$$

where IFT represents the inverse Fourier transform. For the above discussion, the transformation of incident beam can be described by a linear system with the transfer function (TF):

$$H(k_{y,inc}) = r(k_{y,inc} \cos \theta_0 + k_{GPs,0} \sin \theta_0) \quad (3)$$

Besides, in order to perform the optical spatial first-order differentiation computing for this system, its transfer function needs to satisfy $H(k_{y,inc}) \propto ik_{y,inc}$ [41]. Based on the above analysis, we can obtain the transfer function $H(k_{y,inc})$

$$H(k_{y,inc}) = \alpha \cdot ik_{y,inc} \quad (4)$$

where α is defined as a coefficient which affects the amplitude of the reflection beam.

In order to calculate the reflection coefficient $r(k_y)$ of this system, the transfer matrix describing the relationship between the forward and backward fields is used here [42]. We use the reflection

coefficients and transmission coefficients of the GPs at m th interface for 1D surface conductivity discontinuity in Ref. [22]:

$$r_{LR,m} = e^{i\psi} \frac{k_{GPs,L} - k_{GPs,R}}{k_{GPs,L} + k_{GPs,R}}, t_{LR,m} = \frac{2(k_{GPs,L}k_{GPs,R})^{1/2}}{k_{GPs,L} + k_{GPs,R}} \quad (5)$$

where

$$\psi = \frac{\pi}{4} - \frac{2}{\pi} \int_0^\infty \frac{\arctan(k_{GPs,L}u/k_{GPs,R})}{u^2 + 1} du \quad (6)$$

In these equations, $k_{GPsL(R)}$ represents the wave vector of the left (right) side regions of discontinuity, which will be discussed latter. The matching matrices M_m of the m th building block and the propagation matrices P_n of the n th segment are obtained by considering the propagative forward-backward fields [42]:

$$M_m = \begin{pmatrix} r_{LR,m} & t_{RL,m} \\ t_{LR,m} & r_{RL,m} \end{pmatrix}, P_n = \begin{pmatrix} e^{i\delta_n} & 0 \\ 0 & e^{-i\delta_n} \end{pmatrix} \quad (7)$$

where $\delta_n = k_{x,n}d_n = (k_{GPs,n}^2 - k_{GPs,0}^2 \sin^2 \theta_0)^{1/2} d_n$, d_0 is the distance between the incident position and the first interface, d_i is the distance between the last interface and detective position of the reflection beam, and $k_{GPs,n}$ is the GPs wave vector of the n th segment. Here, the scattering parameters are achieved by multiplication of the matching matrices and propagation matrices of every block based on transfer matrix method [42]:

$$S = P_0 \prod_{i=1}^{i=4} M_i P_i \quad (8)$$

For the above discussion, S_{11} , the first row and first column of matrix S , represents the reflection coefficient of the system, and the value of S_{11} is determined by the parameter $k_{GPs,n}$. Therefore, let us consider the wave vector $k_{GPs,n}$ of GPs. In quasi-static approximation, the wave vector $k_{GPs,n}$ of GPs is expressed as [6]:

$$k_{GPs,n} = \frac{2i\omega\epsilon_e}{\sigma_n} \quad (9)$$

where ω is the angular frequency ($\omega = 2\pi/\lambda$, λ is the wavelength of incident beam), σ_n is the surface conductivity of the n th graphene segment. Here, $\epsilon_e = (\epsilon_{upper} + \epsilon_{lower})/2$, where ϵ_{upper} and ϵ_{lower} represent the permittivities of the upper and lower media surrounding the graphene layer, respectively. **For the sake of simplicity, in this study, the background of graphene is set as air ($\epsilon_{upper} = \epsilon_{lower} = 1$).** The surface conductivity of graphene is given by $\sigma_n(\omega, \Gamma, \mu_{c,n}, T) = \sigma_{n,intra}(\omega, \Gamma, \mu_{c,n}, T) + \sigma_{n,inter}(\omega, \Gamma, \mu_{c,n}, T)$ [43], where $\sigma_{n,intra}$ and $\sigma_{n,inter}$ represent the intraband and interband term, Γ is the scattering rate, and T is the temperature, respectively. In the mid-infrared, the intraband conductivity term usually dominates over the interband term, so in this case, it leads to:

$$\sigma_n(\omega, \Gamma, \mu_{c,n}, T) \approx \sigma_{n,intra}(\omega, \Gamma, \mu_{c,n}, T) = \frac{ie^2 k_B T}{\pi \hbar^2 (\omega + i2\Gamma)} \left\{ \frac{\mu_{c,n}}{k_B T} + 2 \ln \left[\exp \left(-\frac{\mu_{c,n}}{k_B T} \right) + 1 \right] \right\} \quad (10)$$

where e is the electronic charge, k_B is Boltzmann constant and \hbar is the reduced Plank's constant. For the sake of simplicity, Γ and T are set to 0.00051423 eV and 300 K in our simulation, respectively. It is easy to see that the surface conductivity of graphene is dependent on chemical potential and it can be dynamically tuned for different requirements. Obviously, the wave vector $k_{GPs,n}$ is influenced by the chemical potential of graphene. The wave vector k_{GPs} calculated by the mode solver method with Lumerical Mode Solutions (triangle marks) and theoretical methods (solid lines) calculated by Eqs. (9–10) are shown in Fig. 1(b). Here, the meshes in the FDTD simulation

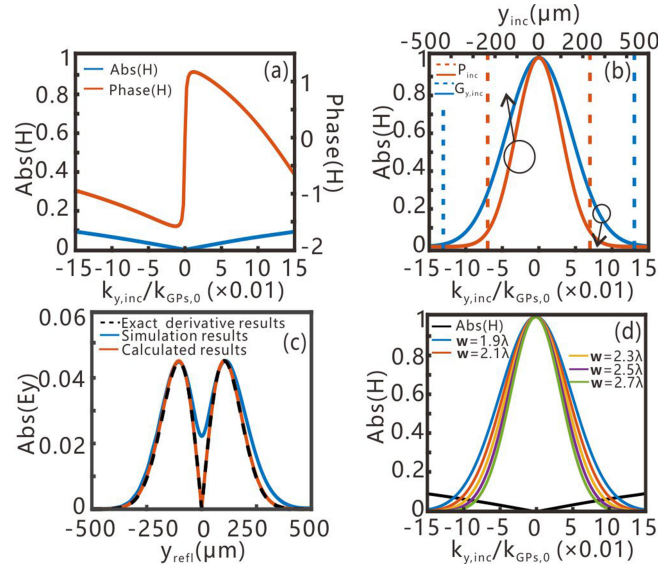


Fig. 2. (a) The absolute value (blue solid line) and phase (red solid line) of TF. (b) The absolute value of the incident beam (red solid line) with $w = 2.1\lambda$ and its angular Fourier spectrum (blue solid line). Vertical dashed lines show the $1/e^2$ level of the beam (red dashed line) and its angular Fourier spectrum (blue dashed line). (c) The absolute value of the reflection beam calculated by simulation method (blue solid line) and theoretical method (orange solid line) based on Eqs. (1)–(10). The exact derivative of incident beam (black dashed line). (d) The angular Fourier spectra of the incident beams with different beam waist sizes w and the absolute value (black solid line) of TF.

are set as $dz = 0.0005 \mu\text{m}$ and the chemical potentials of graphene layers are set as 0.5 eV . Obviously, the simulation results agree very well with the theoretically calculated results. And as the wavelength increases, both the real part and imaginary part of k_{GPs} are reduced correspondingly.

In order to achieve the spatial first-order differentiation, we implement the TF of our proposed structure by analyzing S_{11} in Eq. (8). When the wavelength λ is $70 \mu\text{m}$, Fig. 2(a) shows the angular reflection coefficient spectra with the simulation parameters: $\mu_{c,1} = 0.3836 \text{ eV}$, $\mu_{c,2} = 0.6353 \text{ eV}$, $\mu_{c,3} = 0.6160 \text{ eV}$, $d_1 = 12.7961 \mu\text{m}$, $d_2 = 5.2634 \mu\text{m}$ and $d_3 = 0.9746 \mu\text{m}$. And $\mu_{c,0}$ is fixed as 0.5 eV in our simulation. For a system to implement the first-order differentiation, it is well known that its absolute value of TF should vanish at $k_y = 0$ and TF is a linear function of k_y in the vicinity of the point $k_y = 0$ [11]. In our system, at the minimum, the absolute value (blue solid line) of TF amounts to 3.8×10^{-4} , and TF is approximately a linear function in the vicinity of the point $k_{y,inc} = 0$. Therefore, it is expected to achieve the first-order differentiation in the reflection spectrum based on this structure. Here, it should be noted that the phase (red solid line) does not affect the quality of differentiation and only gives a Goos-Hänchen shift to the reflection beam [12].

Next, in order to demonstrate the optical first-order differentiation supported by our proposed structure, a Gaussian beam $P_{inc}(y_{inc}) = \exp[-(y_{inc}/w)^2]$ is obliquely illuminated on the structure. At this point, beam waist size $w = 2.1\lambda$ is selected and the incident beam spectrum (red solid line) is shown in Fig. 2(b). It should be noted that the beam waist size w of input beam affects the width of the angular Fourier spectrum in the wave vector space. And the angular Fourier spectrum $G(k_{y,inc}) \sim \exp[-(k_{y,inc})^2 w^2/4]$ normalized by its maximum value (blue solid line) is also depicted in Fig. 2(b). Here, the width of the incident beam $P_{inc}(y_{inc})$ and its angular Fourier spectrum $G(k_{y,inc})$ at the $1/e^2$ level is $208 \mu\text{m}$ (red dashed lines) and $g/k_{\text{GPs},0} = 0.12$ (blue dashed lines), respectively. When the angle of incidence is $\theta_0 = 50.23^\circ$, the simulation results (blue solid line) is exhibited in Fig. 2(c). It is detected at the position where is $48 \mu\text{m}$ away from the interface between two graphene segments whose chemical potentials are $\mu_{c,0}$ and $\mu_{c,1}$, respectively. For the sake of contrast, the theoretically calculated results (red solid line) based on Eqs. (1)–(10) and the exact derivative (black dashed line) of incident beam are also shown in Fig. 2(c). We can find that the

TABLE 1
Pearson Correlation Coefficients and the Maximum Amplitudes of Reflection Beam

Beam waist size w	1.9λ	2.1λ	2.3λ	2.5λ	2.7λ
Amplitude	0.0475	0.0452	0.0430	0.0422	0.0409
PCC	0.9603	0.9699	0.9721	0.9790	0.9809

theoretically calculated results agree very well with the exact derivative results. It is observed that there is an obvious difference between the simulation results and theoretically calculated results. It indicates that there still exist a performance gap between our proposed differentiator and an ideal differentiator. We also use the Pearson correlation coefficient (PCC) to measure the linear correlation between the simulation results and the exact derivative results of the incident beam. In this case, PCC is 0.9699, indicating that the simulation results and exact derivative results of the incident beam are quite similar. To understand the effect of beam waist size w , the angular Fourier spectrums of the incident beams with different beam waist sizes are shown in Fig. 2(d). Obviously, as beam waist size w increases, the angular spectrum width g decreases and the TF of the structure is closer to a linear function at the $|k_{y,inc}| \leq g$. This feature affects the PCC and the maximum amplitude of the reflection beam. To show this influence, in terms of different beam waist sizes, the PCC and the maximum amplitude of the reflection beam from the simulation method are recorded in detail. As shown in Table 1, the increase of the Gaussian beam waist size leads to a decrease in the amplitude of the reflection beam, while it leads to an increase in the PCC. At the same time, it can be found that this graphene-based structure can implement the first-order spatial differentiation with the PCC higher than 0.97 when the beam waist size of the incident beam $w > 1.9\lambda$. For a Gaussian beam with the fixed beam waist size, the reflection beam is affected by the feature of TF, which is determined by the slope α and the similarity δ between the current TF and ideal TF. And δ is calculated by:

$$\delta = \sqrt{\sum_{i=1}^n (x_i - y_i)^2} \quad (11)$$

where x_i and y_i represent the value of the current TF and ideal TF. For a fixed α , the differentiation is more ideal when δ is smaller. For a better understanding of the effect of α and δ in our system, with the high tunability of graphene, GA is used to achieve more ideal differentiation by searching more suitable structure parameters (d_1 , d_2 , d_3 , $\mu_{c,1}$, $\mu_{c,2}$ and $\mu_{c,3}$).

3. Inverse Design of the OSD

Firstly, let us consider the TF of our structure by optimizing similarity δ based on GA for $\alpha = 1/3$, $\alpha = 2/3$ and $\alpha = 1$. In order to obtain a more ideal TF of the first-order differentiator, the optimization objective of GA is defined as the similarity δ between the optimized TF and ideal TF. In this work, δ is used as the fitness in GA. Namely, the GA employed here should effectively optimize δ as small as possible. And the parameters choices in GA are as follows: the population size is 100, the maximum genetic generation is 200, the crossover probability is 0.01 and the generation gap is 0.95. In the optimization process of GA, the individuals (structure parameters) are firstly initialized within a certain range, and then they are encoded as the binary numbers in the crossover and mutation processes. When the fitness of each individual is calculated, the structure parameters should be converted to decimal numbers. After that, the selection for the individuals in the population is influenced by the rank of the fitness. As shown in Fig. 3(a), as genetic generation increases, the fitness δ exhibits continuous downtrend, indicating the convergence of GA. In Fig. 3(a), it shows the convergence curves of GA for the TF's slope with $\alpha = 1/3$ (blue line), $\alpha = 2/3$ (red line) and $\alpha = 1$ (orange line), respectively. Finally, δ is optimized to reach the minimum value $\delta = 0.0736$, $\delta = 0.0975$ and $\delta = 0.1257$, respectively. In order to show the optimized results, the optimized

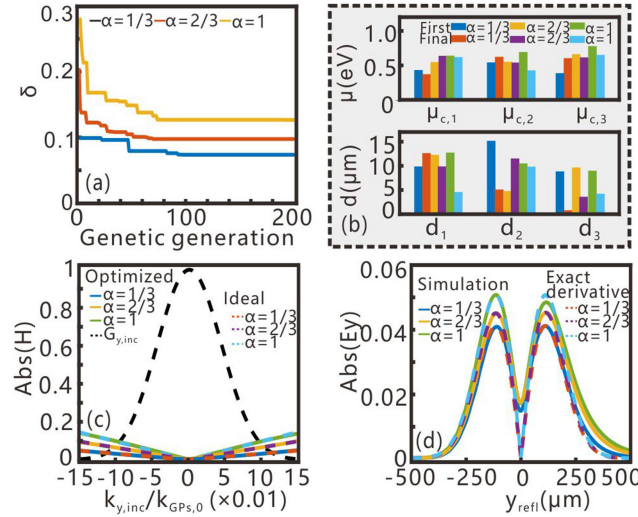


Fig. 3. (a) The convergence curves of GA for $\alpha = 1/3$ (blue line), $\alpha = 2/3$ (red line) and $\alpha = 1$ (orange line), respectively. (b) The structure parameters of the first generation and the final generation for $\alpha = 1/3$, $\alpha = 2/3$ and $\alpha = 1$, respectively. (c) The absolute value of the optimized TFs (solid line) and ideal TFs (dashed line) for $\alpha = 1/3$, $2/3$ and 1 . The angular Fourier spectrum (black dashed line) of the incident beam. (d) The simulation results (solid line) and the exact derivative results (dashed line) for $\alpha = 1/3$, $2/3$ and 1 .

structure parameters (red strips) and the structure parameters of the first generation in GA (blue strips) are both depicted in Fig. 3(b) for $\alpha = 1/3$, $\alpha = 2/3$ and $\alpha = 1$, respectively. Meanwhile, the optimized TF (solid line) and the ideal TF (dashed line) are shown in Fig. 3(c). We can find that the minimum value of TF is close to zero (9.5×10^{-4} , 6.6×10^{-5} and 4.1×10^{-4}) and it is approximately a linear function in the vicinity of the point $k_{y,\text{inc}} = 0$, indicating the optimized structure parameters can realize the TF of an ideal first-order differentiator. To exhibit the performance of the first-order differentiator optimized by GA, the distribution of $\text{abs}(E_y)$ for the reflection beam based on the simulation method (solid line) and the exact derivatives of the incident beams (dashed line) for $\alpha = 1/3$, $2/3$ and 1 are shown in Fig. 3(d). Here, the maximum amplitudes of reflection beam are 0.0409, 0.0450, 0.505 for $\alpha = 1/3$, $2/3$ and 1 , respectively. It indicates that a larger α can lead to a larger maximum amplitude of the reflection beam. Besides, the PCCs between the exact derivatives of the incident beam and simulation results are 0.981, 0.974, 0.962 for $\alpha = 1/3$, $2/3$ and 1 , respectively. It means that a larger α can lead to a smaller PCC because of the increase of δ .

Based on the above discussion, for our proposed structure, PCC and maximum amplitude can't achieve the optimal value at the same time. Next, let us show the advantage of GA to search for the best value of PCC. In other words, the fitness in GA is replaced by the PCC between the optimized reflection beam and ideal reflection beam and the other settings are the same as before. As previously, the convergence curve of the fitness for GA is exhibited in Fig. 4(a). It can be found that the PCC increases obviously from the first generation, but it tends to be a fixed value finally. And the final fitness means that the optimized results have a good agreement with the ideal results. Meanwhile, the structure parameters of the optimized results (red strips) and the first generation (blue strips) in GA are both depicted in Fig. 4(b). **A significant difference is observed between the optimized structure parameters and on-optimized structure parameters.** Similarly, Fig. 4(c) shows the TF with the optimized parameters. Here, the minimum value (blue solid line) is close to zero (8.5×10^{-5}), and it's approximately a linear function in the vicinity of the point $k_{y,\text{inc}} = 0$, indicating the optimized TF is close to the ideal TF of a first-order differentiator. At the same time, the slope of TF ($\alpha \approx 1/5$) and δ ($\delta = 0.0561$) are smaller than the previous results in Fig. 3(c). Let us analyze the performance of the first-order differentiator optimized by GA. For the sake of comparison,

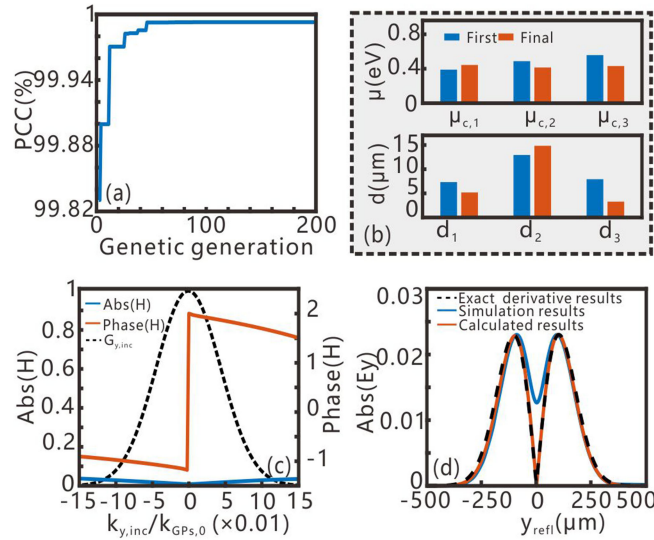


Fig. 4. (a) The convergence curve of GA. (b) The structure parameters of the optimized results (red strips) and the first generation in GA (blue strips). (c) The absolute value (blue solid line) and phase (orange solid line) of the TF with optimized parameters. And the angular Fourier spectrum (black dashed line) of the incident beam. (d) The absolute value of the reflection beam calculated by simulation method (blue solid line) and theoretical method (orange solid line) based on Eqs. (1)–(10). The exact derivative of incident beam (black dashed line).

the distribution of $abs(E_y)$ for the reflection beam from numerical simulation (blue solid line) and theoretical method (orange solid line) are shown in Fig. 4(d). As expected, the maximum amplitude of reflection beam (almost 0.023) is smaller than the previous results, while PCC (0.9882) is higher than previous results (Fig. 3(d)).

Finally, to balance the PCC and the maximum amplitude of the reflection beam, we use GA to optimize the structure for more suitable performance. In the setting of GA, the fitness is changed to be the combination of PCC and the similarity δ between the optimized reflection beam and ideal reflection beam with a weight ratio of 1:1. Here, the weight ratio can be changed according to different performance requirements. And other settings in GA are the same as before. To show the progress of optimization, the convergence curve of the fitness for GA is exhibited in Fig. 5(a). It is shown that the fitness increases obviously from the first generation, but it tends to be a fixed value finally. At this case, the final fitness indicates that the optimized results have a good agreement with the ideal results based on the balance of PCC and the similarity δ between the optimized reflection beam and ideal reflection beam. To show the optimization results of GA, the structure parameters of the optimization results (red strips) and the first generation (blue strips) are both depicted in Fig. 5(b). Meanwhile, the TF with the optimized parameters is shown in Fig. 5(c). The minimum value of the TF (blue solid line) is 3.7×10^{-5} , and it is approximately a linear function in the vicinity of the point $k_{y,inc} = 0$. Moreover, the value of slope is almost 4/5, while δ is 0.1063. For the first-order differentiator optimized by GA, the distribution of $abs(E_y)$ for the reflection beam from numerical simulation (blue solid line) and theoretical method (orange solid line) are shown in Fig. 5(d). We find that the maximum amplitude of reflection beam is 0.0472, and PCC is 0.9755. Based on the previous analysis, these two values are not the optimal values for each other, but are the balance value. To compare our proposed first-order differentiator with the previous structures, the NRMSD between the simulation results and ideal results is calculated here. For this example, the NRMSD amounts to 0.41%, which is almost 0.13% smaller than the previous results (Table 1). And the performance of our proposed first-order differentiator is better than the existed structure [1], [6], [8].

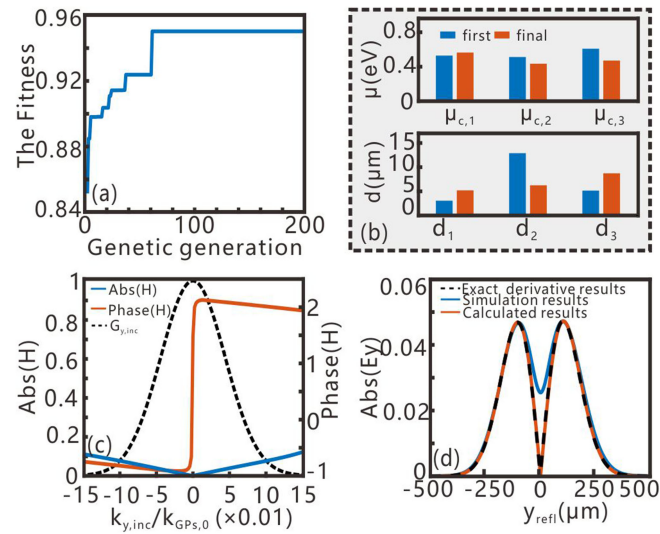


Fig. 5. (a) The convergence curve of GA. (b) The structure parameters of the optimized results (red strips) and the first generation in GA (blue strips). (c) The absolute value (blue solid line) and phase (orange solid line) of the TF with optimized parameters. And the angular Fourier spectrum (black dashed line) of the incident beam. (d) The absolute value of the reflection beam calculated by simulation method (blue solid line) and theoretical method (orange solid line) based on Eqs. (1)–(10). The exact derivative of incident beam (black dashed line).

4. Conclusion

In conclusion, we propose a graphene-based metalines to perform first-order differentiation in terahertz region. The numerical simulation results show that the efficiency of the optical differentiator can reach higher than 97% when beam waist size $w > 1.9\lambda$. With the help of inverse design technology, the maximum amplitude of reflection beam and the similarity between the optimized reflection beam and ideal reflection beam are investigated in detail. The optimization results show that the NRMSD of our proposed first-order differentiator is smaller than previous structures. Obviously, our proposed first-order differentiator optimized by inverse design technology not only proposes a high-performance OSD but also introduces a new way to optimize the photonics devices.

References

- [1] L. L. Doskolovich *et al.*, "Planar two-groove optical differentiator in a slab waveguide," *Opt. Express*, vol. 25, no. 19, pp. 22328–22340, 2017.
- [2] W. Wu *et al.*, "Multilayered analog optical differentiating device: Performance analysis on structural parameters," *Opt. Lett.*, vol. 42, no. 24, pp. 5270–5273, 2017.
- [3] A. Youssefi *et al.*, "Analog computing by Brewster effect," *Opt. Lett.*, vol. 41, no. 15, pp. 3467–3470, 2016.
- [4] N. V. Golovastikov *et al.*, "Analytical description of 3D optical pulse diffraction by a phase-shifted Bragg grating," *Opt. Express*, vol. 24, no. 17, pp. 18828–18842, 2016.
- [5] E. A. Bezus *et al.*, "Spatial integration and differentiation of optical beams in a slab waveguide by a dielectric ridge supporting high-Q resonances," *Opt. Express*, vol. 26, no. 19, pp. 25156–25165, 2018.
- [6] S. AbdollahRamezani *et al.*, "Analog computing using graphene-based metalines," *Opt. Lett.*, vol. 40, no. 22, pp. 5239–5242, 2015.
- [7] A. Silva *et al.*, "Performing mathematical operations with metamaterials," *Science*, vol. 343, no. 6167, pp. 160–163, 2014.
- [8] A. Chizari *et al.*, "Analog optical computing based on a dielectric meta-reflect array," *Opt. Lett.*, vol. 41, no. 15, pp. 3451–3454, 2016.
- [9] Y. Fang, Y. Lou, and Z. Ruan, "On-grating graphene surface plasmons enabling spatial differentiation in the terahertz region," *Opt. Lett.*, vol. 42, no. 19, pp. 3840–3843, 2017.
- [10] T. Zhu *et al.*, "Plasmonic computing of spatial differentiation," *Nat. Commun.*, vol. 8, 2017, Art no. 15391.

- [11] L. L. Doskolovich *et al.*, "Spatial differentiation of Bloch surface wave beams using an on-chip phase-shifted Bragg grating," *J. Opt.*, vol. 18, no. 11, 2016, Art no. 115006.
- [12] Z. Ruan, "Spatial mode control of surface plasmon polariton excitation with gain medium: From spatial differentiator to integrator," *Opt. Lett.*, 40, no. 4, pp. 601–604, 2015.
- [13] D. A. Bykov *et al.*, "Time-domain differentiation of optical pulses in reflection and in transmission using the same resonant grating," *J. Opt.*, vol. 15, no. 10, 2013, Art no. 105703.
- [14] D. A. Bykov, L. L. Doskolovich, and V. A. Soifer, "Temporal differentiation of optical signals using resonant gratings," *Opt. Lett.*, vol. 36, no. 17, pp. 3509–3511, 2011.
- [15] A. B. Clymer, "The mechanical analog computers of Hannibal Ford and William Newell," *IEEE Annals History of Comput.*, vol. 15, no. 2, pp. 19–34, Feb. 1993.
- [16] J. Canny, A computational approach to edge detection, in *Readings in Computer Vision*, New York, NY, USA: Elsevier, 1987, pp. 184–203.
- [17] S. H. Lee *et al.*, "Switching terahertz waves with gate-controlled active graphene metamaterials," *Nat. Mater.*, vol. 11, pp. 936–941, 2012.
- [18] A. Fallahi and J. Perruisseau-Carrier, "Design of tunable biperiodic graphene metasurfaces," *Phys. Rev. B*, vol. 86, 2012, Art no. 195408.
- [19] Y. Yang, J. Zhao, J. Zhou, Z. Liu, and Y. Fu, "Switchable polarization selective terahertz wavefront manipulation in a graphene metasurface," *IEEE Photon. J.*, vol. 11, no. 3, pp. 1–9, Jun. 2019, Art no. 4600909.
- [20] T. Zhang *et al.*, "Dynamically tunable plasmon induced absorption in graphene-assisted metalodielectric grating," *Opt. Express*, vol. 25, no. 21, pp. 26221–26233, 2017.
- [21] S. A. Maier, *Plasmonics: Fundamentals and Applications*, Berlin, Germany: Springer, 2007.
- [22] B. Rejaei and A. Khavasi, "Scattering of surface plasmons on graphene by a discontinuity in surface conductivity," *J. Opt.*, vol. 17, no. 7, 2015, Art no. 075002.
- [23] T. Zhang, L. Chen, and X. Li, "Graphene-based tunable broadband hyperlens for far-field subdiffraction imaging at mid-infrared frequencies," *Opt. Express*, vol. 21, no. 18, pp. 20888–20899, 2013.
- [24] X. Han *et al.*, "Dynamically tunable plasmon induced transparency in a graphene-based nanoribbon waveguide coupled with graphene rectangular resonators structure on sapphire substrate," *Opt. Express*, vol. 23, no. 25, pp. 31945–31955, 2015.
- [25] H. Kwon *et al.*, "Nonlocal metasurfaces for optical signal processing," *Phys. Rev. Lett.*, vol. 121, 2018, Art no. 173004.
- [26] T. J. Davis *et al.*, "Metasurfaces with asymmetric optical transfer functions for optical signal processing," *Phys. Rev. Lett.*, vol. 123, 2019, Art no. 013901.
- [27] H. Babashah *et al.*, "Integration in analog optical computing using metasurfaces revisited: toward ideal optical integration," *J. Opt. Soc. Amer. B*, vol. 34, no. 6, pp. 1270–1279, 2017.
- [28] S. Molesky *et al.*, "Inverse design in nanophotonics," *Nature Photon.*, vol. 12, pp. 659–670, 2018.
- [29] W. Bogaerts and L. Chrostowski, "Silicon photonics circuit design: Methods, tools and challenges," *Laser Photon. Rev.*, vol. 12, 2019, Art no. 1700237.
- [30] K. Yao, R. Unni, and Y. Zheng, "Intelligent nanophotonics: merging photonics and artificial intelligence at the nanoscale," *Nanophotonics*, vol. 8, no. 3, pp. 339–366, 2019.
- [31] T. W. Hughes, M. Minkov, I. A. Williamson, and S. Fan, "Adjoint method and inverse design for nonlinear nanophotonic devices," *ACS Photon.*, vol. 5, pp. 4781–4787, 2018.
- [32] T. W. Hughes, M. Minkov, Y. Shi, and S. Fan, "Training of photonic neural networks through in situ backpropagation and gradient measurement," *Optica*, vol. 5, no. 7, pp. 864–871, 2018.
- [33] B. Shen, P. Wang, R. Polson, and R. Menon, "An integrated-nanophotonics polarization beamsplitter with $2.4 \times 2.4 \mu\text{m}^2$ footprint," *Nat. Photon.*, vol. 9, pp. 378–382, 2015.
- [34] H. Cui, X. Sun, and Z. Yu, "Genetic-algorithm-optimized wideband on-chip polarization rotator with an ultrasmall footprint," *Opt. Lett.*, vol. 42, pp. 3093–3096, 2017.
- [35] Z. Guo *et al.*, "Investigation on three-hump phosphor-coated white light-emitting diodes for healthy lighting by genetic algorithm," *IEEE Photon. J.*, vol. 11, no. 1, Feb. 2019, Art no. 8200110.
- [36] Z. Yu *et al.*, "Inverse-designed low-loss and wideband polarization-insensitive silicon waveguide crossing," *Opt. Lett.*, vol. 44, no. 1, pp. 77–80, 2018.
- [37] T. Zhang *et al.*, "Efficient training and design of photonic neural network through neuroevolution," *Opt. Express*, vol. 27, no. 26, pp. 37150–37163, 2019.
- [38] T. Zhang *et al.*, "Efficient spectrum prediction and inverse design for plasmonic waveguide systems based on artificial neural networks," *Photon. Res.*, vol. 7, no. 3, pp. 368–380, 2019.
- [39] J. Peurifoy *et al.*, "Nanophotonic particle simulation and inverse design using artificial neural networks," *Sci. Adv.*, vol. 4, 2018, Art no. eaar4206.
- [40] T. Zhang *et al.*, Machine learning and evolutionary algorithm studies of graphene metamaterials for optimized plasmon-induced transparency, 2019, *arXiv:1908.01354v3*.
- [41] L. L. Doskolovich *et al.*, "Spatial differentiation of optical beams using phase-shifted Bragg grating," *Opt. Lett.*, vol. 39, no. 5, pp. 1278–1281, 2014.
- [42] S. J. Orfanidis, *Electromagnetic waves and antennas*, 2002.
- [43] G. W. Hanson, "Dyadic Green's functions and guided surface waves for a surface conductivity model of graphene," *J. Appl. Phys.*, vol. 103, 2008, Art no. 064302.